frontiers in Physics

ORIGINAL RESEARCH
published: 25 November 2020
doi: 10.3389/fphy.2020.616349

Defective Titanium Dioxide-supported Ultrasmall Au Clusters for Photocatalytic Hydrogen Production

Xiaoqin Zhang[1], *Wenna Zhang*[1], *Yuanmei Xu*[1,2,3]* *and Mingliang Jin*[1,2]*

[1]National Center for International Research on Green Optoelectronics, South China Academy of Advanced Optoelectronics, South China Normal University, Guangzhou, China, [2]International Academy of Optoelectronics at Zhaoqing, South China Normal University, Guangdong, China, [3]State Key Lab of Silicon Materials, Zhejiang University, Hangzhou, China

Ultrasmall precious metal clusters have attracted extensive attention for providing a very specific surface and promoting electron transfer. In this work, ultrasmall Au clusters based on defective TiO_2 nanosheets (Au/D-TiO_2) were prepared and introduced into photocatalytic hydrogen evolution. Different defects of TiO_2 nanosheets (D-TiO_2) were constructed using a heating process and then loaded with Au clusters. Compared with bare TiO_2, Au clusters established on defective TiO_2 nanosheets with a narrower band gap showed higher light absorption performances, resulting in obviously enhanced photocatalytic hydrogen production performances. The Au/D-TiO_2 displayed the greatly enhanced photocatalytic hydrogen evolution activity of 3,142.33 $\mu mol\ h^{-1}\ g^{-1}$, which was over 45 times than the pure TiO_2. The results showed that the catalysts had good prospects in the field of photocatalytic hydrogen production.

Keywords: Au, cluster, defect TiO_2, H_2 evolution, photocatalytic

OPEN ACCESS

Edited by:
Chongfu Zhang,
University of Electronic Science and Technology of China, China

Reviewed by:
Xiaolei Wang,
University of Alberta, Canada
Yongchao Huang,
Guangzhou University, China

***Correspondence:**
Mingliang Jin
jinml@scnu.edu.cn
Yuanmei Xu
yuanmei.xu@ecs-scnu.org

Specialty section:
This article was submitted to Optics and Photonics, a section of the journal Frontiers in Physics

Received: *12 October 2020*
Accepted: *02 November 2020*
Published: *25 November 2020*

Citation:
Zhang X, Zhang W, Xu Y and Jin M (2020) Defective Titanium Dioxide-supported Ultrasmall Au Clusters for Photocatalytic Hydrogen Production. Front. Phys. 8:616349. doi: 10.3389/fphy.2020.616349

1. INTRODUCTION

Photocatalytic H_2 evolution, which utilizes water decomposition under solar energy, is a promising route to overcome the growing energy crisis and environment issues. However, in this process, the photocatalyst plays a key role. At present, photocatalysts such as nitrides [1, 2], metal sulfides [3, 4], and metal oxides [5, 6] have been demonstrated in hydrogen evolution systems. Among the traditional photocatalysts, anatase is one of the most extensively studied photocatalysts due to its reasonable price, nontoxicity, and remarkable photochemical stability [7, 8]. However, TiO_2 with a comparatively large band gap (3.2 eV) can absorb only the ultraviolet portion of the solar spectrum, resulting in insufficient photocatalytic activity of TiO_2 for H_2 production.

Photocatalytic efficiency of TiO_2 for water decomposition is limited due to the high recombination rate of photogenerated carriers. Hence, many measures have been taken to solve the problem of low photocatalytic performance of TiO_2, involving the mingling of transition metals [9, 10], adding of the nonmetal ions [11, 12], loading of the precious metals [13, 14], the surface for dye-sensitized [15], and the generation of hybrid semiconductor [16, 17]. The manufacture of metal-semiconductor oxide composite materials is another very dynamic research area that can improve the photocatalytic activity of semiconductor oxide photocatalysts [18]. It has been reported that the transfer of electrons from semiconductor oxides to metals may reduce electron hole recombination events and improve the photocatalytic performances of semiconductor oxide-based catalysts. Thus, the electron hole pairs in the recombined semiconductor oxide produced by photons can be reduced by a large part [19, 20].

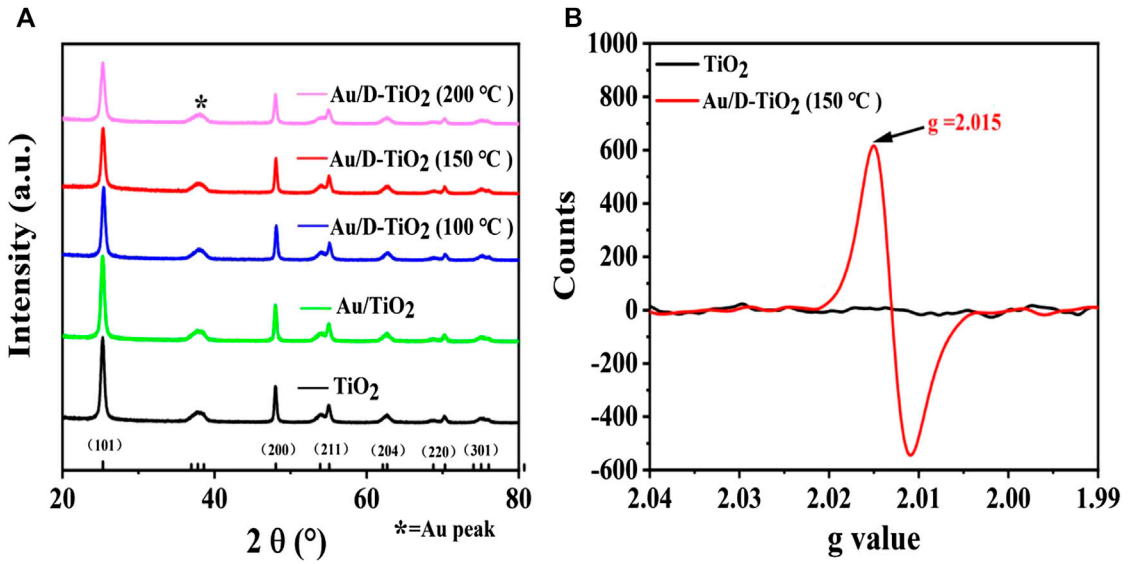

FIGURE 1 | (A) XRD of pure TiO_2, Au/TiO_2, and Au/D-TiO_2 (The D-TiO_2 were treated at 100°, 150°, and 200°C, respectively) **(B)** EPR of TiO_2 and Au/D-TiO_2 (treated at 150°C).

Therefore, in this work, the electron hole recombination rate was reduced, we have demonstrated a method of constructing defects on metal oxides to support Au clusters. Both oxygen vacancies and a Ti-O-Ti structure were formed in this process. Oxygen atoms were lost through the formed oxygen vacancies, and the original oxygen vacancies were occupied by metal clusters, thus effectively reducing the recombination rate of photogenerated carriers. Au clusters built on defective TiO_2 nanosheets (Au/D-TiO_2) were applied to the production of photocatalytic hydrolysis hydrogen and showed significantly enhanced performances. Compared with the traditional TiO_2 catalyst, the catalysts of Au/D-TiO_2 could produce up to 45 times more hydrogen than TiO_2. The results demonstrated that the structural defects on the surface of metal oxide could improve the catalytic performance of Au/D-TiO_2 catalysts. This work laid a foundation for the preparation of catalysts in the future.

2. EXPERIMENTAL SECTION

2.1. Materials

The chemical reagents Tetra-n-butyl Titanate ($Ti(OC_4H_9)_4$, 99.0%, AR grade), hydrofluoric acid solution (HF, 40.0 wt%, AR grade), ethanol (99.7%, AR grade), and ammonium carbonate (40%, AR grade) were bought from Tianjin Damao Chemical Reagent Factory, China. $HAuCl_4{\cdot}3H_2O$ (99.9%, AR grade) was bought from Aladdin, China. All experimental materials were used directly in the experiment after purchase.

2.2. Sample Preparation

2.2.1. Preparation of D-TiO_2 Nanosheets

TiO_2 nanosheets were obtained by hydrothermal method. In a common synthesis, $Ti(OC_4H_9)_4$ (50 ml) and HF (6 ml) were added to the Teflon-lined autoclave. Then, the hydrothermal reaction occurred at 180°C for 24 h. After the reaction, the white sediment of the Teflon-lined autoclave was centrifuged and rinsed three times with water and ethanol, and dried in an oven at a temperature of 80°C for 12 h. Different defects of D-TiO_2 sample were obtained after being calcined at reducing atmosphere (10 vol.% H_2 and 90 vol.% Ar, 2 h) with unequal temperatures (The D-TiO_2 were treated at 100°, 150°, and 200°C, respectively).

2.2.2. Synthesis of Au/D-TiO_2

Au/D-TiO_2 was composite according to the deposition-precipitation method. First, 1 g of pure or defective TiO_2 nanosheets powders were suspended in 50 ml distilled water and stirred for 20 min. Then, the aqueous solution (25 ml) of 2.4 g $(NH_4)_2CO_3$ and 0.01 g $HAuCl_4{\cdot}3H_2O$ were mixed into the above solution drop by drop and stirred for 1 h at room temperature. And then, the samples were collected by centrifugation, and washed with distilled water and ethanol for three times, respectively. Au/D-TiO_2 samples were gained after being dried at 70°C for 6 h and calcined (200°C, 10 vol.% H_2 and 90 vol.% Ar) for 2 h. For comparison, Au/TiO_2 was synthesized with the same method on TiO_2 nanosheets instead of D-TiO_2.

2.2.3. Characterization

The crystalline structures of the acquired samples were analyzed by a powder X-ray diffractometer (XRD, BRUKER D8 ADVANCE) with a scan range of 10°–90° and a step size of 0.02°. The measurement of electron paramagnetic resonance (EPR) was performed at room temperature using a BRUKE A300 EPR spectrometer. The transmission electron microscopy (TEM) and high angle annular dark-field (HAADF) were performed on a JEM-2100HR operating at

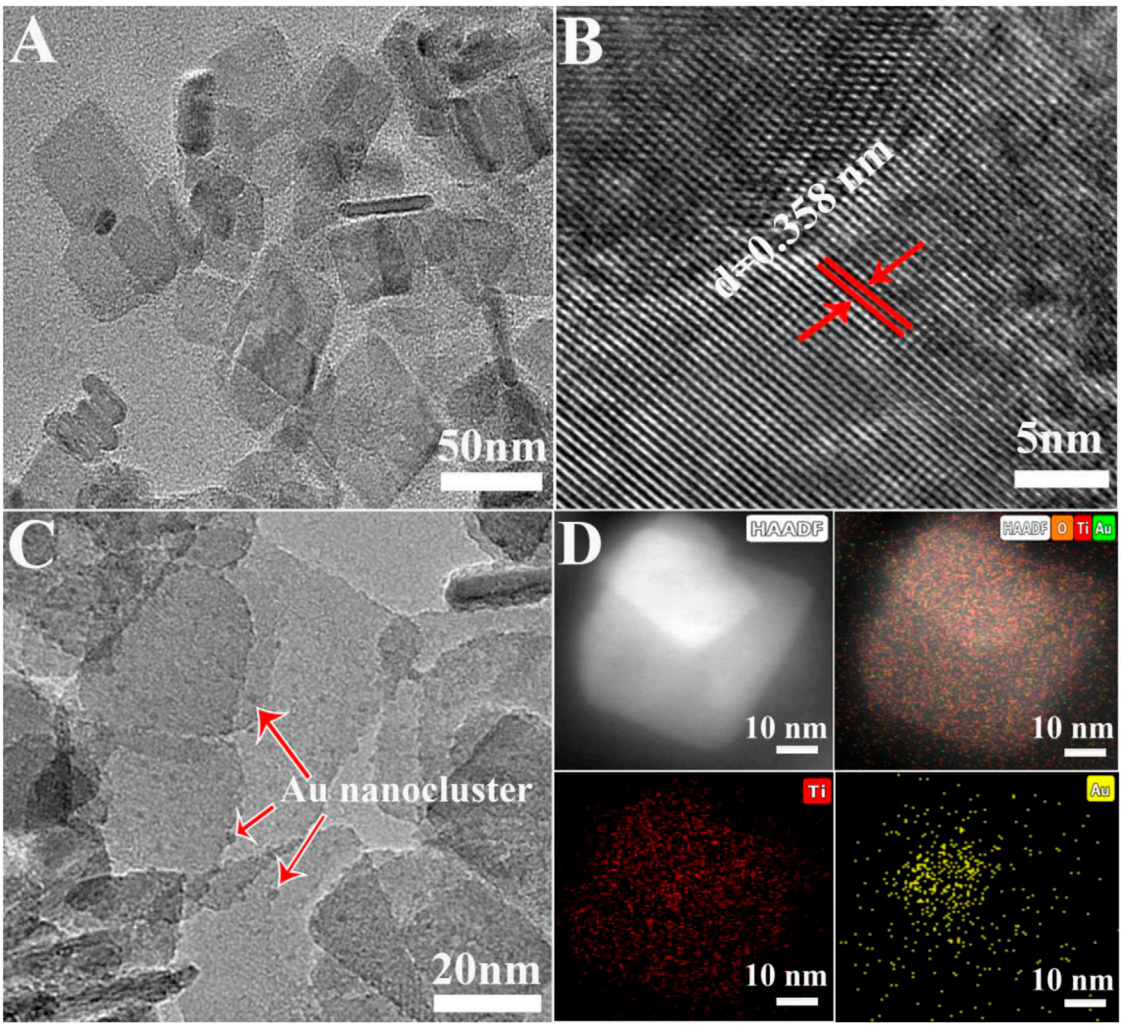

FIGURE 2 | (A) TEM image of TiO_2 nanosheets **(B)** HRTEM image of the selective area **(C)** TEM image, Au clusters high-lighted by red arrows **(D)** elemental mappings show the distribution of Ti (red) and Au (gold).

200 kV. The surface analysis of every sample was examined by X-ray photoelectron spectroscopy (XPS) using a Thermo Fisher Scientific K-Alpha spectrometer. The Metal contents of samples were analyzed by analysis of inductively coupled plasma spectroscopy (ICP, Agilent 700). The UV-vis diffuse reflectance spectra (DRS) recorded on a Lambda 750 spectrophotometer. The photoluminescence (PL) spectra gained by a F-4600 FL Spectrophotometer.

2.2.4. Photocatalytic Hydrogen Evolution

The photocatalytic hydrolysis reaction was carried out in a heat-resistant glass reactor, which was connected to a sealed single channel glass system, a circulating water system, a controller, and a vacuum pump. A 300 w xenon lamp was applied as a light source and fixed with the distance of 1 cm from the glass reactor. The glass reactor was charged with 80 ml of distilled water, 20 ml of methanol solution and 50 mg of photocatalyst. Before the start of the reaction, in order to keep the entire reaction device free of air, the vacuum pump was turned on for 1 h, and the valves of the glass system were rotated while evacuating, and the air of the system was extracted as much as possible. The circulating water and the controller were opened while the vacuum pump was being punched, and the magnetic stirrer placed under the glass reactor was turned at 500 rpm to avoid overheating of the reaction during the experiment and to guarantee uniform dispersion of the photocatalyst in the solution. In the photocatalytic hydrogen production experiment, a gas chromatograph was used to analyze the produced hydrogen gas, and the gas chromatograph was equipped with a packed bed column having a temperature of 70°C and a detector. In the hydrogen production experiment, the xenon lamp irradiation time was 1 h for each time, and the intake air was detected every hour with a total of 4 h [21, 22].

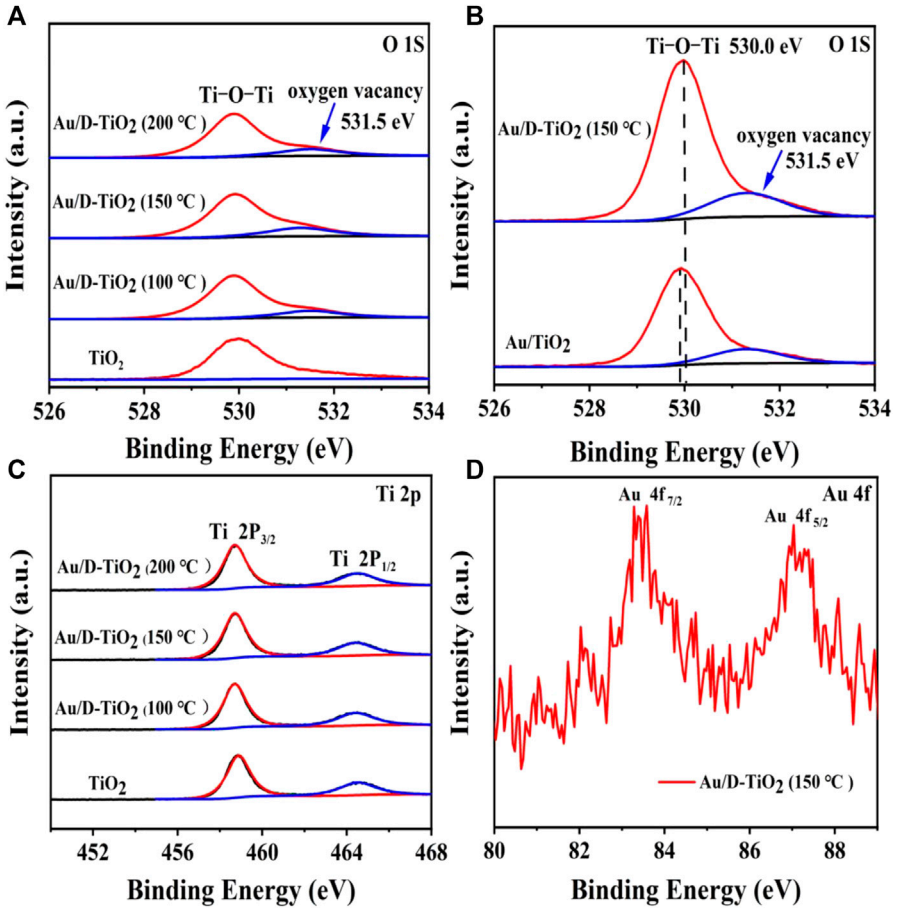

FIGURE 3 | (A) XPS of TiO_2 and D-TiO_2 (The D-TiO_2 were treated at 100˚, 150˚, and 200˚C, respectively) **(B)** XPS of synthesized Au/TiO_2 and Au/D-TiO_2 (treated at 150˚C) **(C)** Ti 2p spectrum **(D)** Au 4f spectrum.

3. RESULTS AND DISCUSSION

The compositions and phase structures of the samples were studied by using XRD (**Figure 1**). It could be seen from the XRD patterns that both pure and defective TiO_2 were with a palpable structure of anatase phase (JCPDS no. 21-1272). In the case of Au/D-TiO_2, the crystallographic peaks of Au could be detected (**Figure 1A**). Defects in D-TiO_2 were tested by electron paramagnetic resonance (EPR) measurements (**Figure 1B**), which indicated an aerobic vacancy defect with a g value of 2.015 [23–25].

The preparation of defective TiO_2 was the first and an important step in the synthesis process of the catalyst Au/D-TiO_2. The transmission electron microscopy (TEM) image (**Figure 2A**) demonstrated the nanosheet structure of D-TiO_2 with a length of about 50 nm. And the high-resolution transmission electron microscopy (HRTEM) showed a lattice spacing of approximate 0.358 nm (**Figure 2B**) corresponding to (101) planes of TiO_2. In addition, **Figure 2C** had many Au clusters distributed and marked by the red arrow. Further, the high angle annular dark-field (HAADF) and the element mapping image (**Figure 2D**) further indicated that the Au clusters were well dispersed on the defective TiO_2 carrier.

In order to further explore the surface defects of the pure TiO_2 and the defective TiO_2, the X-ray photoelectron spectroscopy (XPS) spectra were conducted. The O 1 score-level XPS spectrum manifested two peaks in **Figure 3A**, one of which at 530.0 eV was considered as the oxygen band of Ti-O-Ti, and another one at 531.5 eV could be attributed to oxygen vacancy. The peak area of 531.5 eV of 150˚C treated sample was larger than that of the other samples, indicating the highest oxygen vacancy concentration (**Figure 3A**). **Figure 3B** showed the O 1 s XPS spectrum of Au/TiO_2 and Au/D-TiO_2 (treated at 150˚C). It was found that the binding energy of Au/D-TiO_2 was significantly shifted to higher binding energies compared with Au/TiO_2. And the strength of Ti-O-Ti of Au/D-TiO_2 (treated at 150˚C) was greater than that of Au/TiO_2. Usually, such binding energy transfer is explained by a strong interaction between the two components. **Figure 3C** displayed the Ti 2p XPS spectrum of TiO_2 and Au/D-TiO_2 (The D-TiO_2 were treated at 100˚, 150˚, and 200˚C, respectively) and demonstrated that they

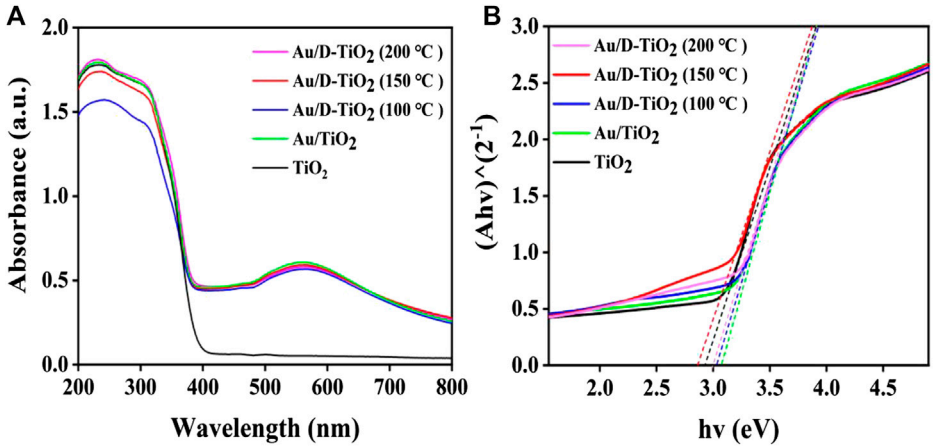

FIGURE 4 | (A) UV-vis DRS of synthesized of TiO_2, Au/TiO_2 and Au/D-TiO_2 (The D-TiO_2 were treated at 100°, 150°, and 200°C, respectively) **(B)** the forbidden band width of synthesized of TiO_2, Au/TiO_2, and Au/D-TiO_2 (The D-TiO_2 were treated at 100°, 150°, and 200°C, respectively).

were not obvious differences. The Au 4f of Au/D-TiO_2 (treated at 150°C) core-level XPS spectrum displayed one special peak at 83.9 eV in **Figure 3D**, and this peak could be attributed to Au clusters [26, 27].

The measurements of UV-visible diffuse-reflectance spectrum (UV-vis DRS) were carried out to investigate the light absorption intensity. As can be seen from **Figure 4A**, the intensity of light absorption for Au/D-TiO_2 was significantly enhanced in the wavelength ranging from 250 to 800 nm compared with the untreated TiO_2 nanosheets. And Au/D-TiO_2 (treated at 150°C) showed the strongest absorption intensity. According to the UV-vis DRS, the optical band gap value E_g of all samples was estimated from these absorption profiles using the Tauc's relation (**Figure 4B**) [28]. As shown in **Figure 4B**, the band gaps of these samples were analogous. However, after combining with Au clusters, the band gap of the samples mildly narrowed, whereby the results of pure TiO_2, Au/TiO_2, Au/D-TiO_2 (treated at 100°C), Au/D-TiO_2 (treated at 150°C) and Au/D-TiO_2 (treated at 200°C) were 2.93, 3.05, 3.03,2.86 and 2.98 ev, respectively [29, 30].

Figure 5 presented a comparison of the PL spectra of synthesized TiO_2 and Au/D-TiO_2 (The D-TiO_2 were treated at 100°, 150°, and 200°C, respectively). PL emission in semiconductors was due to the recombination of free carriers. The PL peak at about 396 nm was attributed to the emission of the bandgap transition. At an excitation wavelength of 230 nm, the light energy was approximately equal to the bandgap energy of anatase (387 nm). As expected, the PL intensity of the prepared Au/D-TiO_2 was significantly reduced as compared with pure TiO_2. This indicated that the recombination rate of electrons and holes of Au/D-TiO_2 sample was low. This might be owing to the fact that electrons were excited from the valence band to the conduction band, and then moved to Au, thereby preventing the direct recombination of electrons and holes. In general, low recombination rate of electrons and holes are often associated with high photocatalytic activity [31, 32].

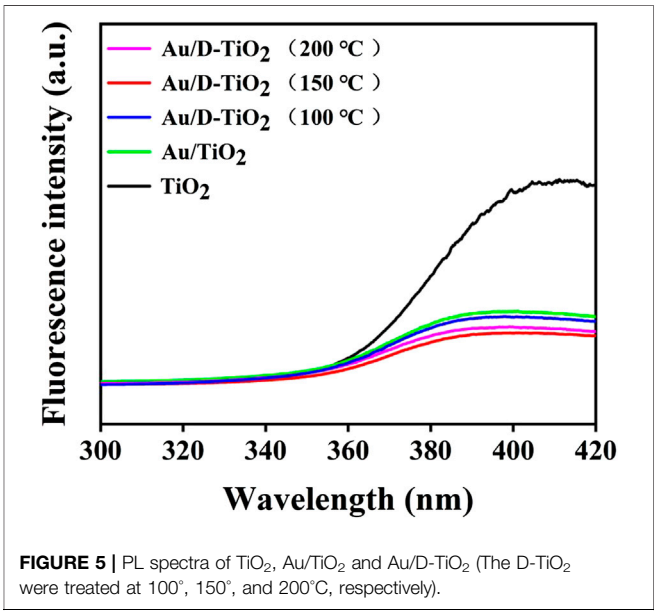

FIGURE 5 | PL spectra of TiO_2, Au/TiO_2 and Au/D-TiO_2 (The D-TiO_2 were treated at 100°, 150°, and 200°C, respectively).

In order to understand the band structure change of TiO_2 nanosheets after Au loading, the Mott-Schottky experiment (MS) was conducted (**Figure 6**).

Based on the MS equation, the capacitance (C) depend on applied potential and could be fitted as follows [33]:

$$\frac{1}{C^2} = + \frac{2}{e\varepsilon\varepsilon_0 N_d}\left(E - E_{FB} - \frac{k_b}{e}\right) \quad (1)$$

Where the slope expresses the type of semiconductor (negative to p-type and positive to n-type). The N_d denotes the carrier density. The *C*, *E* (corrected by the AgCl vs 0.197 eV) denote the space charge capacitance and applied potential. ε denotes the relative permittivity. ε_0 denotes the vacuum permittivity. Where *e*

denotes the electron charge. Besides, the intercept on the x axis denotes the E_{fb} (band potential).

As revealed in **Figure 6**, the positive slope in the Mott–Schottky plot for the samples indicated that TiO_2 nanosheets was typical n-type semiconductors according to the MS equation. Furthermore, the conduction band (CB) of the samples were obtained corrected by the AgCl by calculating, and the flat band potential (E_{fb} (Vs RHE)) of pure TiO_2, Au/TiO_2, Au/D-TiO_2 (treated at 100°C), Au/D-TiO_2 (treated at 150°C) and Au/D-TiO_2 (treated at 200°C) were gained to be −0.16, −0.13, −0.07, −0.04, and −0.01 V, respectively. Moreover, the valence band (VB) was calculated by adding the band gap value to the CB level. whereby the results of pure TiO_2, Au/TiO_2, Au/D-TiO_2 (treated at 100°C), Au/D-TiO_2 (treated at 150°C) and Au/D-TiO_2 (treated at 200°C) were 2.77, 2.92, 2.96, 2.82, and 2.97 V, respectively compared with NHE.

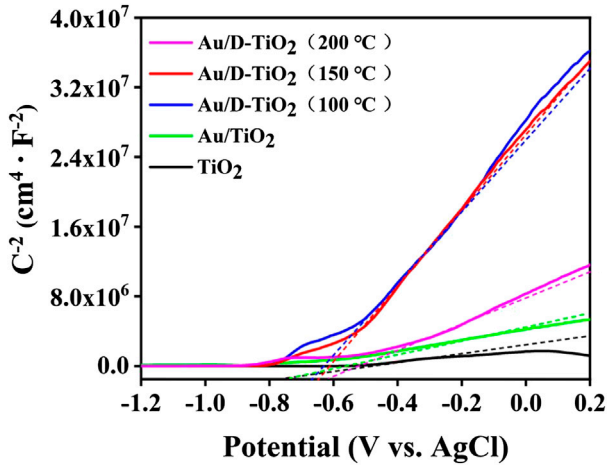

FIGURE 6 | The Mott–Schottky curves of using Ag/AgCl as a reference electrode of TiO_2, Au/TiO_2, and Au/D-TiO_2 (The D-TiO_2 were treated at 100°, 150°, and 200°C, respectively).

The photocatalytic H_2 production activities of the bare TiO_2, Au/TiO_2 and Au/D-TiO_2 were further examined in **Figure 7**. Under the same experimental conditions, the test was performed every 1 h, and a total of 4 h of experiments were performed. Bare TiO_2 and Au/TiO_2 only exhibited a very low photocatalytic H_2 production rate of 69.18 and 138.7 $\mu mol\, h^{-1}\, g^{-1}$, respectively. However, after coupling with Au clusters, the production rate of photocatalytic H_2 was significantly enhanced. Au/D-TiO_2 (treated at 150°C) exhibited the highest photocatalytic H_2 production rate of 3,142.33 $\mu mol\, h^{-1}\, g^{-1}$, suggesting that the construction of Au/D-TiO_2 could effectively boost the production activity of photocatalytic H_2. Besides, the production rate of photocatalytic H_2 first increased and then declined when the treated temperature of D-TiO_2 increased from 100° to 200°C for Au/D-TiO_2 samples, indicating that the treated temperature could efficiently adjust the defects of TiO_2 nanosheets and effect the H_2 production activity [34–36].

The stability test with Au/D-TiO_2 was carried out by a total of 16 h of cycling experiments, which were divided into four groups of 4 h, respectively, and an injection was performed every hour for data recording. The result suggested a good stability of Au/D-TiO_2 at fully photocatalytic hydrogen production experiment process without obvious decrease, which might be due to the Au clusters could be effectively stabilized on TiO_2.

A reaction mechanism for the evolution of hydrogen is shown in **Figure 8**. First, the valence band electrons of TiO_2 are excited to the conduction band, and then immediately transferred to Au through the intimate interface contacts. Since it is well known that H_2O has an ionization balance in the natural state, the water contains trace amounts of H^+ and OH^-. Therefore, the releasing H^+ binding in the e^- of H_2O to produce H_2. H^+ adsorption on the surface of the Au and accepting excited electrons is a key step in the

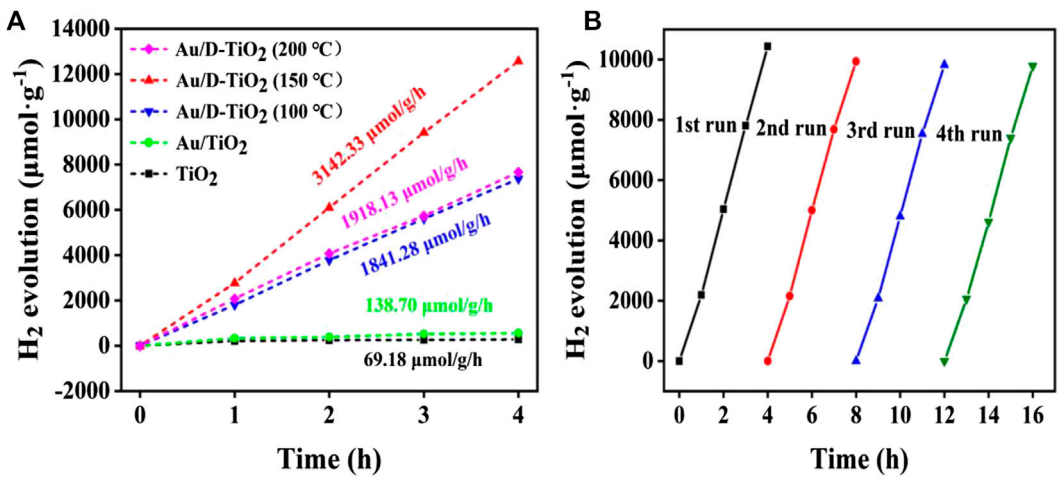

FIGURE 7 | (A) H_2 production of TiO_2, Au/TiO_2, and Au/D-TiO_2 (The D-TiO_2 were treated at 100°, 150°, and 200°C, respectively) under sunlight irradiation **(B)** Circulation experiment of hydrogen evolution of Au/D-TiO_2 (treated at 150°C).

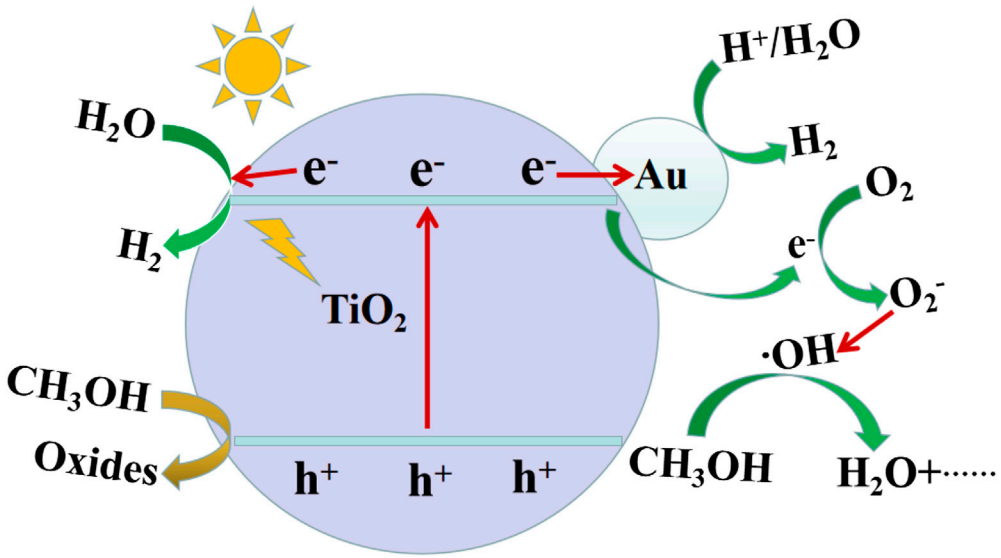

FIGURE 8 | Schematic diagram of charge transfer and H_2 production of Au/D-TiO_2.

hydrogen evolution reaction. On the other hand, H_2O/OH^- reacts with h^+ in Au/D-TiO_2 to produce H_2 and OH. When H_2 is released, O_2 is also formed. Then O_2 reacts with the e^- to form O_2^-. Finally, the O_2^- reacts with CH_3OH to form H_2O. When TiO_2 is coupled with Au clusters, it can provide more active sites for the hydrogen release reaction due to the characteristics of the Au/D-TiO_2 catalyst, thereby increasing photocatalytic activity [37, 38].

CONCLUSION

In conclusion, Au based on defective TiO_2 nanosheets (Au/D-TiO_2) has been successfully prepared and applied to the production of photocatalytic hydrolysis hydrogen. Compared with bare TiO_2 and Au/TiO_2 only exhibit a very low production rate of photocatalytic H_2 of 69.18 and 138.7 μmol h^{-1} g^{-1}, respectively, the production rate of photocatalytic H_2 was significantly enhanced after coupling with Au clusters. The Au/D-TiO_2 treated at 150°C exhibited the highest production rate of photocatalytic H_2 of 3,142.33 μmol h^{-1} g^{-1}. The stability test suggested a good stability of Au/D-TiO_2 at fully photocatalytic hydrogen production experiment process due to the Au clusters could be effectively stabilized on TiO_2. Overall, this could be an effective approach for enhancing photocatalytic hydrogen production efficiency and stability by catalyst.

DATA AVAILABILITY STATEMENT

The original contributions presented in the study are included in the article/supplementary material, further inquiries can be directed to the corresponding authors.

AUTHOR CONTRIBUTIONS

XZ: Conducted experiments and wrote manuscript; WZ: Conducted experiments, evaluated data; YX: Designed experiments, evaluated data, and revised manuscript; MJ: Acquired research funding, conceived research and revised manuscript.

FUNDING

This work was financially supported by Guangdong Provincial Grant (2018A050506025), Special Fund Project of Science and Technology Application in Guangdong (2017B020240002), Guangdong Provincial Key Laboratory of Optical Information Materials and Technology (Grant No. 2017B030301007), Guangdong Innovative Research Team Program (No. 2016ZT06C517), Science and Technology Program of Guangzhou (No. 2019050001).

REFERENCES

1. Li L, Yu H, Xu J, Zhao S, Liu Z, Li Y. Rare earth element, Sm, modified graphite phase carbon nitride heterostructure for photocatalytic hydrogen production. *New J Chem* (2019) 43:1716–24. doi:10.1039/C8NJ05619F
2. Ismael M, Wu Y, Wark M. Photocatalytic activity of ZrO_2 composites with graphitic carbon nitride for hydrogen production under visible light. *New J Chem* (2019) 43:4455–62. doi:10.1039/C8NJ06507A
3. Liang Q, Cui S, Xu S, Yao C, Maclachlan MJ, Li Z. A porous triptycene-based covalent polymer stabilized binary metal sulfide for enhanced hydrogen evolution under visible light. *Chem Comm* (2018) 54:3391–4. doi:10.1039/C8CC00665B
4. Zhang K, Guo L. Metal sulphide semiconductors for photocatalytic hydrogen production. *Catal Sci Technol* (2013) 3:1672. doi:10.1039/C3CY00018D
5. Martha S, Sahoo PC, Parida KM. An overview on visible light responsive metal oxide based photocatalysts for hydrogen energy production. *RSC Adv* (2015) 5:61535–53. doi:10.1039/C5RA11682A

6. Tian H, Cui X, Zeng L, Su L, Song Y, Shi J. Oxygen vacancy-assisted hydrogen evolution reaction of the Pt/WO_3 electrocatalyst. *J Mater Chem A* (2019) 7: 6285–93. doi:10.1039/C8TA12219A
7. Kumaravel V, Mathew S, Bartlett J, Pillai SC. Photocatalytic hydrogen production using metal doped TiO_2: a review of recent advances. *Appl Catal B Environ* (2019) 244:1021–64. doi:10.1016/j.apcatb.2018.11.080
8. Salimi M, Behbahani M, Sobhi HR, Gholami M, Jafari AJ, Kalantary RR, et al. A new nano-photocatalyst based on Pt and Bi co-doped TiO_2 for efficient visible-light photo degradation of amoxicillin. *New J Chem* (2019) 43:1562–8. doi:10.1039/C8NJ05020A
9. Yunarti RT, Lee M, Hwang YJ, Choi J, Suh DJ, Lee J, et al. Transition metal-doped TiO_2 nanowire catalysts for the oxidative coupling of methane. *Catal Commun* (2014) 50:54–8. doi:10.1016/j.catcom.2014.02.026
10. Kim J, Kwon G, Lim H, Zhu C, You H, Kim Y. Effects of transition metal doping in Pt/M-TiO_2 (M = V, Cr, and Nb) on oxygen reduction reaction activity. *J Power Sources* (2016) 320:188–95. doi:10.1016/j.jpowsour.2016.04.091
11. Li Y, Xu D, Oh JI, Shen WZ, Li X, Yu Y. Mechanistic study of codoped titania with nonmetal and metal ions: a case of C + Mo codoped TiO_2. *ACS Catal* (2012) 2:391–8. doi:10.1021/cs2006668
12. Yang G, Wang T, Yang B, Yan Z, Ding S, Xiao T. Enhanced visible-light activity of F-N co-doped TiO_2 nanocrystals via nonmetal impurity, Ti^{3+} ions and oxygen vacancies. *Appl Surf Sci* (2013) 287:135–42. doi:10.1016/j.apsusc.2013.09.094
13. Tian F, Zhu R, Ouyang F. Synergistic photocatalytic degradation of pyridine using precious metal supported TiO_2 with $KBrO_3$. *J Environ Sci* (2013) 25: 2299–305. doi:10.1016/S1001-0742(12)60304-0
14. Walsh FC, Bavykin DV, Torrentemurciano L, Lapkin AA, Cressey BA. Synthesis of novel composite materials via the deposition of precious metals onto protonated titanate (TiO_2) nanotubes. *Trans IMF* (2013) 84: 293–9. doi:10.1179/174591906X149077
15. Ooyama Y, Uenaka K, Sato T, Shibayama N, Ohshita J. Effective co-sensitization using D–π–A dyes with a pyridyl group adsorbing at Brønsted acid sites and Lewis acid sites on a TiO_2 surface for dye-sensitized solar cells. *RSC Adv* (2015) 5:2531–5. doi:10.1039/C4RA14190C
16. Fajariah N, Prabowo WA, Fathurrahman F, Melati A, Dipojono HK. The investigation of electronic structure of transition metal doped TiO_2 for diluted magnetic semiconductor applications: a first principle study. *Procedia Eng* (2017) 170:141–7. doi:10.1016/j.proeng.2017.03.032
17. Boga B, Szekely I, Pap Z, Baia L, Baia M. Detailed spectroscopic and structural analysis of TiO_2/WO_3 composite semiconductors. *J Spectrosc* (2018) 2018: 6260458. doi:10.1155/2018/6260458
18. Song S, Cheng B, Wu N, Meng A, Cao S, Yu J. Structure effect of graphene on the photocatalytic performance of plasmonic Ag/Ag_2CO_3-rGO for photocatalytic elimination of pollutants. *Appl Catal B Environ* (2016) 181: 71–8. doi:10.1016/j.apcatb. 2015.07.034
19. Efimkin DK, Burg GW, Tutuc E, MacDonald AH. Tunneling and fluctuating electron-hole Cooper pairs in double bilayer graphene. *Phys Rev B* (2020) 101: 035413. doi:10.1103/PhysRevB.101.035413
20. Prades JD, Hernandezramirez F, Jimenezdiaz R, Manzanares M, Andreu T, Cirera A, et al. The effects of electron–hole separation on the photoconductivity of individual metal oxide nanowires. *Nanotechnol* (2008) 19:465501. doi:10.1088/0957-4484/19/46/465501
21. Qi K, Lv W, Khan I, Liu S. Photocatalytic H_2 generation via CoP quantum-dot-modified g-C_3N_4 synthesized by electroless plating. *Chin J Catal* (2020) 41: 114–21. doi:10.1016/S1872-2067(19)63459-5
22. Reddy NR, Bhargav U, Kumari MM, Cheralathan KK, Shankar MV, Reddy KR, et al. Highly efficient solar light-driven photocatalytic hydrogen production over Cu/FCNTs-titania quantum dots-based heterostructures. *J Environ Manag* (2020) 254:109747. doi:10.1016/j.jenvman.2019.109747
23. Liu Q, Wang F, Lin H, Xie Y, Tong N, Lin J, et al. Surface oxygen vacancy and defect engineering of WO_3 for improved visible light photocatalytic performance. *Catal Sci Technol* (2018) 17:399–406. doi:10.1039/C8CY00994E
24. Alsaad AM, Al-Bataineh QM, Qattan IA, Ahmad AA, Ababne A, Bataineh Z, et al. Measurement and ab-initio investigation of structural, electronic, optical and mechanical properties of sputtered aluminium nitrides thin films. *Front Phys* (2020) 8:115. doi:10.3389/fphy.2020.00115
25. Ye K, Li K, Lu Y, Guo Z, Ni N, Liu H, et al. An overview of advanced methods for the characterization of oxygen vacancies in materials. *Trends Anal Chem* (2019) 116: 102–8. doi:10.1016/j.trac.2019.05.002
26. Zhang Z, Qin J, Shi W, Liu Y, Zhang Y, Liu Y, et al. Enhanced power conversion efficiency of perovskite solar cells with an up-conversion material of Er^{3+}-Yb^{3+}-Li^{+} tri-doped TiO_2. *Nanoscale Res Lett* (2018) 13:147. doi:10.1186/s11671-018-2545-y
27. Criado A, Lavela P, Ortiz GF, Tirado JL, Gzouli S, Edfouf Z, et al. CTAB-assisted synthesis of C@$Na_3V_2(PO_4)_2F_3$ with optimized morphology for application as cathode material for Na-ion batteries. *Front Phys* (2019) 7: 207. doi:10.3389/fphy.2019.00207
28. Xu Y, Zhang H, Li X, Wang W, Li J. Ag-encapsulated single-crystalline anatase TiO_2 nanoparticle photoanodes for enhanced dye-sensitized solar cell performance. *J Alloys Compd* (2017) 95:1104–11. doi:10.1016/j.jallcom.2016.10.236
29. Wang S, Li C, Wang T, Zhang P, Li A, Gong J. Controllable synthesis of nanotube-type graphitic C_3N_4 and their visible-light photocatalytic and fluorescent properties. *J Mater Chem A* (2014) 2:2885. doi:10.1039/C3TA14576J
30. Xu Y, Zhang H, Li X, Wu Q, Wang W, Li Z, et al. Investigation of the improved performance with ferrites in TiO_2 dye-sensitized solar cell. *Appl Surf Sci* (2017) 424:245–50. doi:10.1016/j.apsusc.2017.04.210
31. Hisatomi T, Takanabe K, Domen K. Photocatalytic water-splitting reaction from catalytic and kinetic perspectives. *Catal Lett* (2014) 145:95–108. doi:10.1007/s10562-014-1397-z
32. Yu X, Wang Y, Meng X, Yang J. Preparation and characterization of Pd/N codoped TiO_2 photocatalysts with high visible light photocatalytic activity. *Chin J Catal* (2013) 34:1418–28. doi:10.1016/S1872-2067(12)60597-X
33. Martin DJ, Reardon PJ, Moniz SJ, Tang J. Visible light-driven pure water splitting by a nature-inspired organic semiconductor-based system. *J Am Chem Soc* (2014) 136:12568–71. doi:10.1021/ja506386e
34. Akple MS, Low J, Wageh S, Alghamdi AA, Yu J, Zhang J, et al. Enhanced visible light photocatalytic H_2-production of g-C_3N_4/WS_2 composite heterostructures. *Appl Surf Sci* (2015) 358:196–203. doi:10.1016/j.apsusc.2015.08.250
35. Li K, Lu X, Zhang Y, Liu K, Huang Y, Liu H Bi_3TaO_7/Ti_3C_2 heterojunctions for enhanced photocatalytic removal of water-borne contaminants. *Environ Res* (2020) 185:109409. doi:10.1016/j.envres.2020.109409
36. Wei W, Tian Q, Sun H, Liu P, Zheng Y, Fan M, et al.. Efficient visible-light-driven photocatalytic H_2 evolution over MoO_2-C/CdS ternary heterojunction with unique interfacial microstructures. *Appl Catal B Environ* (2020) 260: 118153. doi:10.1016/j.apcatb.2019.118153
37. Xu Y, Wang X, Jin M, Kempa K, Shui L. Water splitting performance enhancement of the TiO_2 nanorod array electrode with ultrathin black phosphorus nanosheets. *Chem Electro Chem* (2019) 7:96–104. doi:10.1002/celc.201901456
38. Huang Y, Guo Z, Liu H, Zhang S, Wang P, Lu J, et al. Heterojunction architecture of N-doped WO_3 nanobundles with Ce_2S_3 nanodots hybridized on a carbon textile enables a highly efficient flexible photocatalyst. *Adv Funct Mater* (2019) 29:45. doi:10.1002/adfm.201903490

Conflict of Interest: The authors declare that the research was conducted in the absence of any commercial or financial relationships that could be construed as a potential conflict of interest.